

# Flow noise estimation models for axial flow past towed sonar arrays

**Rakesh Sekharipuram Sekar**  
Student

Department of Mechanical Engineering  
Indian Institute of Technology Palakkad  
Kanjikode, Palakkad, Kerala, 678623  
India  
Email: 132203001@smail.iitpkd.ac.in

**Senthil Rajan S**  
Scientist

Naval Physical and Oceanographic Laboratory  
Kochi, Kerala, 682021  
India  
Email: senthilrajan.npol@gov.in

**Dr. Anoop Akkoorath Mana\***  
Assistant Professor

Department of Mechanical Engineering  
Indian Institute of Technology Palakkad  
Kanjikode, Palakkad, Kerala, 678623  
India  
Email: akkoorath@iitpkd.ac.in

*Towed sonar arrays house a series of pressure sensors inside a fluid-filled elastic tube. Towing of the sonar array in water generates a turbulent boundary layer on the exterior surface of the elastic tube. The pressure fluctuations in the turbulent boundary layer along with other ambient pressure fluctuations, excites the elastic tube and further generates pressure disturbances in the interior fluid. In this work, a new semi-empirical model of the turbulent pressure spectrum is presented. The new model predictions show a closer agreement with the available experimental results at all tow speeds. A three-dimensional vibroacoustic model of the fluid-filled elastic tube is also presented in this work. The vibroacoustic model is fully coupled and considers both breathing mode and first order variations in the elastic tube and the acoustic field variables. Further, the turbulent pressure spectrum semi-empirical model and the three-dimensional vibroacoustic model are used to compute the on-axis sound pressure level due to the external turbulent pressure excitation at different elastic tube diameters and tow speeds. At low frequencies, increasing tube diameter has little ef-*

*fect on flow noise, while at higher frequencies, flow noise decreases with larger diameters. Increasing tow speed raises flow noise across all frequencies.*

## NOMENCLATURE

- A You may include nomenclature here.  
 $\alpha$  There are two arguments for each entry of the nomenclature environment, the symbol and the definition.

The primary text heading is boldface and flushed left with the left margin. The spacing between the text and the heading is two line spaces.

## 1 INTRODUCTION

Towed sonar arrays contain a series of pressure sensors enclosed within a fluid-filled elastic tube. As the sonar array is towed through the water, a thick layer of turbulent flow is generated over the exterior surface of the tube. The pressure fluctuations in this turbulent boundary layer (TBL), along with other ambient sea pressure variations, excite the elastic tube and subsequently produce

---

\* Address all correspondence related to ASME style format and figures to this author. Address all correspondence for other issues to this author.

acoustic pressure disturbances within the interior fluid. The hydrophones placed in the interior fluid pick these acoustic signals. The signals associated with the turbulent pressure fluctuations are called flow noise. Currently, the flow noise is measured either by towing the sonar array in open water using a dinghy or by allowing the hydrophone to free fall in water [1]. In the first case, noise from the boat and vibrations of the towline connections pollute the measured acoustic signals [2]; whereas in the second case, the useful measurements can be made only at the terminal velocity of the hydrophone. This work aims at developing a fully coupled vibroacoustic model for predicting the flow noise in towed sonar arrays which is useful over wide range of towing speeds and tube diameters.

A widely used model for predicting the turbulent pressure spectrum is that developed by G M Corcos [3] for the flow over a flat plate. In this model, the turbulent pressure is varying exponentially with respect to both the axes of the flat plate. Although this model is widely used in engineering applications, it has a major shortcoming that it is overestimating the pressure level at low wavenumbers. D M Chase [4] presented a simpler turbulent pressure spectrum model for the flow over a flat plate. The model is based on experimental observations and uses direct dependence on the flow and dimensional parameters. Frendi et al. [5] analysed the Corcos [3] model and proposed a turbulent model for the flow over a flat plate based on large eddy simulation (LES) and direct numerical simulation (DNS) computational results. Frendi's model involves the use of an auto spectrum which was derived by Michael Goody [6]. The Frendi model predictions are found to match well with an earlier experimental result on flow over a flat plate. Some of the observations of the Chase and Frendi models are relevant to the present work and are discussed in section 2. Roni Francis et al. [7] used LES and Reynolds averaged Navier Stokes (RANS) computational method to study the wavenumber frequency spectrum of the turbulent pressure field over a flat plate. This work presents an exhaustive discussion on similar problems in the literature.

D M Chase [4] developed a model for computing the turbulent pressure spectrum for an axial flow past a cylinder by modifying his earlier flat plate model. While modifying, Chase considered the radius of the cylinder as one of the parameters instead of the length of the flat plate. Chase derived azimuthal harmonic spectral density by integrating the turbulent pressure spectrum of the flat plate in the cross-flow direction. The details of this model are presented in section 2.1.

A L Carpenter et al. [8] conducted experiments for

finding the flow noise inside a fluid-filled elastic tube while towed behind a ship and compared the results with that predicted by Chase [4]. The authors also proposed a tube transfer function for computing the flow noise inside the tube. Andrew Knight [9] performed similar analytical simulations as in [8] but with different types of hydrophones and compared the flow noise with that for an ideal hydrophone. The ideal hydrophone was assumed to have unit acoustic response and zero convective response. This paper also uses an approximate tube transfer function to find the noise inside the fluid-filled elastic tube.

Unnikrishnan et al. [2] performed experiments to measure the turbulent pressure field outside the elastic tube by towing the sonar array in a quiet lake at different speeds. The work presents a comparison of the experimental results with the available semi-empirical model predictions. It was found that the semi-empirical model estimations match with the measurements only at high tow speeds. Karthik et al. [10] studied the turbulent pressure spectrum over a cylinder with the help of an LES computational model. The model predictions match well with the experimental results of Unnikrishnan et al. [2]. Karthik et al. also presented a non-dimensional turbulent flow noise spectrum for easy estimation of the spectrum at different tow speeds and tube diameters.

Both Carpenter et al. [8] and Andrew Knight [9] estimated the flow noise inside a fluid-filled elastic tube with the help of the Chase model for the turbulent pressure spectrum and an approximate tube transfer function. Ji-neesh et al. [11] developed a better axisymmetric model of the fluid-filled elastic tube and used it to estimate the flow noise inside the tube. It was found that the earlier approximate transfer function model overestimates the flow noise inside the tube.

This paper develops a new semi-empirical model for the turbulent pressure spectrum of axial flow past a solid cylinder. It also presents a fully coupled three-dimensional vibroacoustic model of a fluid-filled elastic tube. Furthermore, these models are used to compute the on-axis sound pressure level resulting from external turbulent pressure excitation on the elastic tube. The organization of the paper is as follows: Section. 2 discusses two existing semi-empirical models for estimating turbulent pressure spectrum for axial flow past a solid cylinder. Section. 3 discusses the development of a new semi-empirical model for the turbulent pressure spectrum, which provides improved predictions compared to existing models. Section. 4 discusses the development of a three-dimensional vibroacoustic model to estimate the on-axis flow noise inside a fluid-filled elastic tube. Further, Section. 5 discusses the estimation of interior acoustic pressure spectrum and on-axis flow noise inside a

fluid-filled elastic tube and are compared with the existing results.

## 2 REVIEW OF SEMI-EMPIRICAL MODELS OF TURBULENT PRESSURE SPECTRUM

One of the aim of this study is to predict the flow noise resulting from turbulent boundary layer excitation. To achieve this, a semi-empirical model that can estimate the turbulent pressure exerted by fluid flow on a cylindrical tube, is required. Two existing semi-empirical models for turbulent pressure fluctuation is discussed in this section. Furthermore, flow noise at the outer surface of the solid cylinder is estimated using these models, showing its variation in comparison to available experimental results [2].

### 2.1 Chase model

Chase [4] proposed a semi-empirical model for predicting the frequency-wavenumber spectrum of turbulent pressure field over a solid cylinder and is given by

$$\hat{p}_0(k_z, \omega) = C \rho^2 \nu_*^3 R^2 \left[ (k_z R)^2 + \frac{1}{12} \right] \times \left[ \frac{(\omega R - u_c k_z R)^2}{h^2 \nu_*^2} + (k_z R)^2 + b_1^{-2} \right]^{-2.5}. \quad (1)$$

The important parameters in the above equation are axial wavenumber  $k_z$ , frequency  $\omega$ , density of the fluid  $\rho$ , convective speed  $u_c$  ( $= 0.68u$ , where  $u$  is the tow speed),  $C = 0.063$ ,  $h = 3.7$ ,  $\nu_* = 0.04U$  and tube radius  $R$  [4] [8] [9] [12] [13].

### 2.2 Frendi model

Frendi's turbulent pressure spectrum for a flat plate is given by

$$\hat{R}(k_z, k_2, \omega) = C_1 R^*(\omega) e^{-\hat{\alpha} r_k}. \quad (2)$$

In the above equation,  $C_1$  is given by

$$C_1 = \alpha^2 m \delta^2 \frac{1}{2\pi}, \quad (3)$$

where  $\alpha$  can be computed using

$$\alpha = \frac{a_1}{\pi} \frac{1}{\sqrt{1 + a_2 \left( \frac{\omega \delta}{u_t} - 50 \right)^2}}. \quad (4)$$

In the above equation,  $a_1 = 4.7$ ,  $a_2 = 3 \times 10^{-5}$  [5],  $u_t$  is the friction velocity ( $= 0.04u$ , a small fraction of tow velocity  $u$ ) and  $\delta$  is the boundary layer thickness [14] given by

$$\delta = [48 Re_a^{-1} Re_x^{(0.0226 \log Re_a + 0.2478)}]^{1/0.91}, \quad (5)$$

where  $Re_a$  is the radius based Reynold's number ( $\frac{\rho u R}{\mu}$ ) and  $Re_x$  is length based Reynold's number ( $\frac{\rho u x}{\mu}$ ),  $x$  is distance of the point of concentration on the cylinder from the leading edge and  $\mu$  is the dynamic viscosity of the fluid medium. The constant  $m$  in Eq. (3) is a scaling factor which is approximately taken as  $1/7.7$  [5].

$R^*(\omega)$  in Eq. (2) is the auto-spectrum given by [6]

$$R^*(\omega) = \frac{3\tau_w^2 \omega^2 \left( \frac{\delta}{u} \right)^3}{[(\frac{\omega \delta}{u})^{0.75} + 0.5]^{3.7} + [1.1 R_t^{-0.57} (\frac{\omega \delta}{u})]^{0.7}}. \quad (6)$$

In the above equation,  $\tau_w$  is the shear stress at the wall.  $R_t$  is the ratio of time scale [6] given by

$$R_t = \left( \frac{u_t}{u} \right) \left( \frac{u_t \delta}{\nu} \right), \quad (7)$$

where  $\nu$  is the kinematic viscosity.

$\hat{\alpha}$  in Eq. (2) is given by  $\hat{\alpha} = \alpha \delta$  and  $r_k$  depends on the axial and crossflow wavenumbers and is given by

$$|r_k^2| = (k_z - \frac{\omega}{u_c})^2 + (m k_2)^2. \quad (8)$$

In the above equation,  $k_z$  denotes the axial wavenumber and  $k_2$  denotes the cross flow wavenumber,  $\omega$  is the frequency and  $u_c$  is the convective speed ( $= 0.68u$ , a large fraction of tow speed  $u$ ). Eq. (2) can be modified for estimating turbulent pressure spectrum for an axial flow past a solid cylinder as

$$\hat{p}_0(k_z, \omega) = \int_{-1/2R}^{1/2R} \hat{R}(k_z, k_2, \omega) dk_2. \quad (9)$$

The estimation of flow noise using the models discussed in this section and its comparison with the findings of experiments is discussed in the next section.

### 2.3 Flow noise

In this section, the estimation of flow noise, as measured by a series of hydrophones placed at the outer surface of a solid cylinder, is discussed and compared with

the experimental results [2]. The flow noise associated with the turbulent pressure spectrum  $p_0(k_z, \omega)$  as registered by an array of hydrophones [2] is

$$Q(\omega) = \int_{-\infty}^{\infty} \hat{p}_0(k_z, \omega) H(k_z) dk_z. \quad (10)$$

In the above equation,  $H(k_z)$  is the hydrophone response function. The hydrophone array is a set of large number of similar elements with specific length arranged at a fixed distance apart. This array acts as noise filter and its response is given by [2]

$$H(k_z) = \frac{\sin(k_z d N / 2)}{N \sin(k_z d / 2)} \frac{\sin(l k_z / 2)}{l k_z / 2}, \quad (11)$$

where  $N$  is the number of hydrophone elements in the array,  $d$  is the distance between two hydrophones and  $l$  is the length of individual hydrophones.

The sound pressure level (SPL) associated with the flow noise ( $Q(\omega)$ ) is given by

$$SPL = 10 \log_{10} \left( \frac{Q(\omega)}{p_{ref}^2} \right). \quad (12)$$

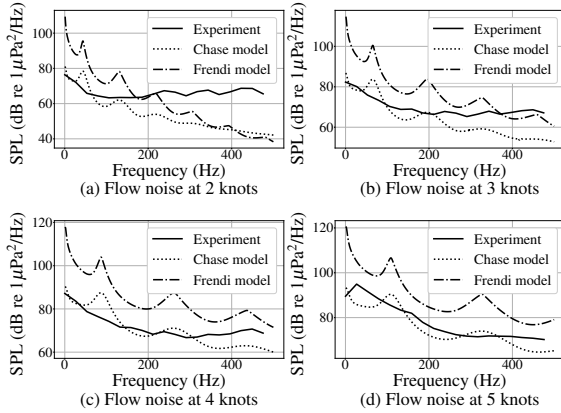


Fig. 1. Comparison of flow noise predicted by Chase [4] and Frendi [5] models with the experimental results [2] at different tow speeds.

Figure 1 compares the flow noise estimated by the Chase [4] and Frendi [5] models with the experimental

results [2] at various tow speeds for a solid cylinder having a diameter of 0.01 m. The sonar array consists of 66 hydrophones, each of length 8 mm, placed at the outer surface of the cylinder with an interval of 16 mm. It is evident from Fig. 1 that the Frendi model consistently overestimates the flow noise at almost all frequencies and tow speeds, whereas the Chase model aligns well with experiments at high tow speeds. However, at low speeds, there is a significant difference between the Chase model and the experiment, especially at high frequencies. Regardless of tow speed, both the models predicts a significant reduction in the flow noise with frequency compared to the experimental results. To address these differences, a new model of turbulent pressure spectrum is proposed in this work to better match the experimental data, particularly at low tow speeds. The development of this new model is discussed in the following section.

### 3 A NEW SEMI-EMPIRICAL MODEL OF THE TURBULENT PRESSURE SPECTRUM

It is shown in the previous sections that the Chase and Frendi models show significant deviation from the experimental results [2] at low tow speeds and at high frequencies. In this section, a new semi-empirical model of the turbulent pressure spectrum is developed that closely aligns with the experimental results [2]. This new model is derived using the insights from both the Chase and the Frendi models, and is referred to as the “hybrid model”.

#### 3.1 The hybrid model

In the “hybrid model”, the pressure spectrum from the Chase [4] model (section. 2.1) is used in conjunction with the exponential decay function present in the Frendi [5] model (section. 2.2). Accordingly, the turbulent pressure spectrum is given by

$$\hat{p}(k_z, k_2, \omega) = C_3 \bar{P}(\omega) e^{-\hat{\alpha} r_k}. \quad (13)$$

In the above equation, the autospectrum  $\bar{P}(\omega)$  is given by

$$\bar{P}(\omega) = \int_{-\infty}^{\infty} \hat{p}_0(\omega, k_z) dk_z, \quad (14)$$

where  $\hat{p}_0(\omega, k_z)$  is the same as that used in the Chase model (Eq. (1)). In this new model, the wavenumber dependency is included in the form of an exponential func-

tion  $e^{-\hat{\alpha}r_k}$ , where  $\hat{\alpha} = \alpha\delta$  with

$$\alpha = \frac{a_1}{\pi} \frac{1}{\sqrt{1 + a_2(\frac{\omega\delta}{u_t} - 50)^2}}, \quad (15)$$

$$\delta = [48Re_a^{-1}Re_x^{(0.0226 \log Re_a + 0.2478)}]_{0.91}^{\frac{1}{0.91}} \quad (16)$$

and

$$|r_k^2| = (k_z - \frac{\omega}{u_c})^2 + (mk_2)^2. \quad (17)$$

In Eq. (15),  $a_1$  and  $a_2$  determine the behaviour of spectrum at low and high frequencies, respectively. It has been observed in Fig. 1 that, the predictions of the Frendi model deviate more at higher frequency ranges. Therefore, the value of  $a_2$  is decreased from  $3 \times 10^{-5}$  to  $3 \times 10^{-6}$ . Different values of  $a_1$  and  $C_3$  were tested to match the experimental results given in Fig. 1. A better match is found with the experimental data when  $a_1 = 1$  and  $C_3 = 1 \times 10^{-4}$ . Further, the turbulent pressure spectrum given in Eq. (13) is integrated over the cross-flow wavenumber  $k_2$  from  $-1/2R$  to  $1/2R$  [4] to obtain the pressure spectrum  $\hat{p}_0(k_z, \omega)$  for axial flow past a solid cylinder. Thus,

$$\hat{p}_0(k_z, \omega) = \int_{-1/2R}^{1/2R} \hat{p}(k_z, k_2, \omega) dk_2. \quad (18)$$

In the next section, the flow noise outside the cylinder is computed using the new hybrid model and the results are compared with existing models and Unnikrishnan's experimental results [2].

### 3.2 Flow noise

The flow noise using the new hybrid model can be computed by Eq. (10). Here, the hybrid model (Eqs. (13)-(18)) is used to compute the turbulent pressure spectrum  $\hat{p}_0(k_z, \omega)$  and Eq. (11) is used for the hydrophone response function  $H(k_z)$ .

A comparison of flow noise measured in SPL (see Eq. (12)) computed using the new hybrid model, Chase model [4] and Unnikrishnan's experiment [2] are shown in Fig. 2. It can be seen that the new hybrid model's predictions match with the measured values [2] at all frequencies and towing speeds. Although, the hybrid model underpredicts noise at high frequencies for the 2 knots

case, the predictions are better than that by the existing Chase and Frendi models.

A comparison of the turbulent pressure spectrum  $\hat{p}_0(k_z, \omega)$  given by the hybrid model (Eqs. (13)-(18)), the Chase model (Eq. (1)) and the Frendi model (Eq. (9)) for a tow speed of 2 knots for different frequencies are shown in Fig. 3. The other parameters used to obtain the plot are the diameter of the cylinder which is chosen as 10 mm [2], density of the fluid is 1000 kg/m<sup>3</sup> and the computation is done at 11 m from the leading edge of the solid cylinder. For a given frequency, at low wavenumbers, the

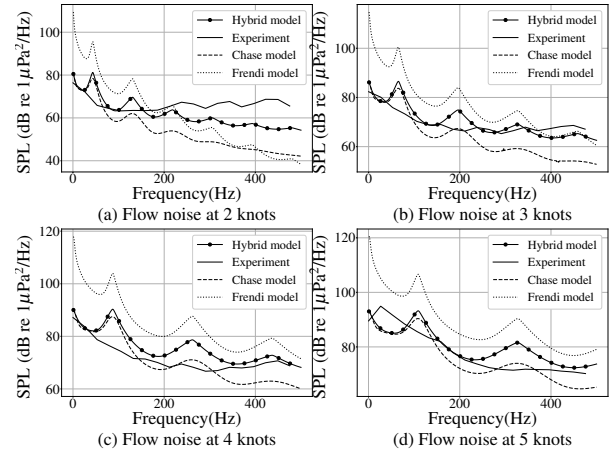


Fig. 2. A comparison of flow noise predicted by the hybrid model, the Chase model [4] and Frendi model [5] with that measured from experiments [2] at different tow speeds.

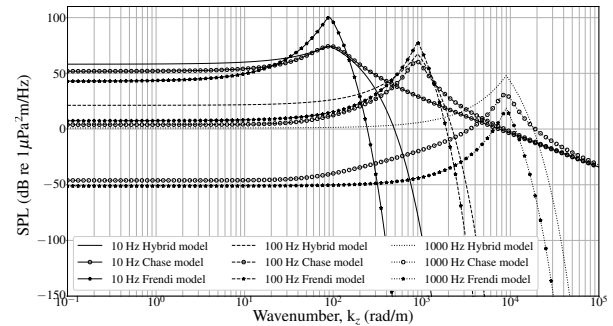


Fig. 3. A comparison of the turbulent pressure spectrum  $\hat{p}_0(k_z, \omega)$  given by the hybrid model (Eq. (18)), Chase (Eq. (1)) and Frendi (Eq. (9)) model at 2 knots.

turbulent pressure spectrum increases at a slow rate. It

peaks at convective wavenumber  $k_c (= \omega/u_c)$  forming a convective ridge. It can be seen that while all the models predicts a ‘flat’ spectrum at lower wavenumbers and a ridge at convective wavenumber, their predictions differ significantly at large wavenumbers. The presence of an exponential function results in an exponential decrease in the spectrum at large wavenumbers for the hybrid and Frendi models. Chase model predicts a higher spectrum with smaller slope at large wavenumbers. It can be seen from Fig. 3 that the predictions by the three models are closer at lower frequencies. However, at high frequencies, the hybrid model predicts a higher spectrum than the rest. This difference in the spectrum predicted by the hybrid model helps to achieve a closer agreement with the measured flow noise as shown in Fig. 2.

### 3.3 Non-dimensional power spectral density

The non-dimensional power spectral density,  $Q_{ND}$ , of flow noise is defined as

$$Q_{ND} = \frac{Q(\omega)}{\rho^2 D U^3}, \quad (19)$$

where  $Q(\omega)$  is the flow noise given by Eq. (10) and  $D$  is the cylinder diameter. The non-dimensional power spectral density calculated using the hybrid model Eqs. (13)-(18) at different tow speeds are shown in Fig. 4. It can be

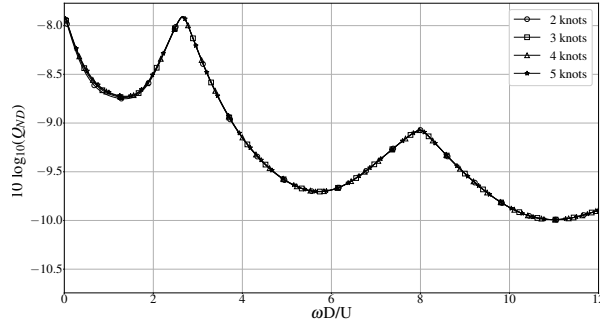


Fig. 4. Non-dimensional power spectral density for different tow speeds using the new hybrid model.

seen that, the non-dimensional power spectral density for different tow speeds collapse to a single curve against the non-dimensional frequency  $\omega D/u$ . One can obtain the power spectral density at different tow speeds and cylinder diameters using this ‘single’ non-dimensional curve.

This section presented a new model of turbulent pressure field for axial flow past a solid cylinder and found

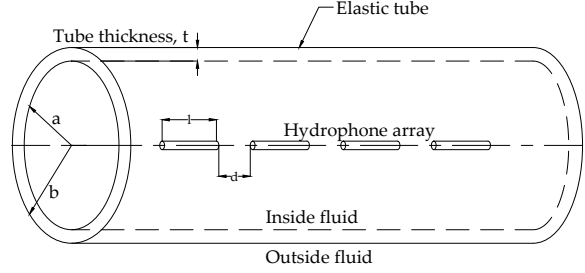


Fig. 5. Fluid filled elastic tube.

that the model predictions are closer to an experimental results [2]. It was assumed that the cylinder is rigid and therefore the pressure field is not altered by the cylinder displacement field. However, the cylindrical tube in towed sonar arrays are not rigid and can be assumed to be elastic. The turbulent pressure fluctuation outside the elastic tube, creates vibration inside the tube and in turn generates acoustic waves in the fluid inside the tube. The next section presents a three-dimensional vibroacoustic model of a fluid-filled elastic tube, which is used in conjunction with the hybrid model for the external turbulent pressure excitation to estimate on-axis flow noise.

## 4 THREE-DIMENSIONAL VIBROACOUSTIC MODEL OF A FLUID-FILLED ELASTIC TUBE

This section develops a fully coupled three-dimensional vibroacoustic model of the fluid-filled elastic tube. A schematic of fluid-filled tube is shown in Fig. 5. First, the displacement field of the elastic tube is derived from the Navier-Lame equilibrium equation (see section. 4.1) and the acoustic pressure field inside the tube is derived from the acoustic wave equation (see section. 4.2). The structure (elastic tube) and the fluid (interior fluid) are then coupled with the help of stress and displacement boundary conditions at the interface (see section. 4.3). The external pressure excitation is also accounted in the form of stress boundary condition at the outer surface of the tube. The boundary conditions, when expressed in terms of the unknown displacement and pressure fields, form a system of linear algebraic equations. The unknown displacement and pressure fields can be computed by solving this system of equations (see section. 4.4).

### 4.1 The elastic tube displacement and stress fields

This section involves modelling of elastic tube using Navier-Lame’s equilibrium equation [15] in three-



dimensional cylindrical coordinates. The Navier-Lame equilibrium equation is given by

$$\mu \nabla^2 \mathbf{U}(r, \theta, z, t) + (\lambda + \mu) \nabla \nabla \cdot \mathbf{U}(r, \theta, z, t) = \rho_s \ddot{\mathbf{U}}(r, \theta, z, t), \quad (20)$$

where  $\mathbf{U}$  is the displacement vector ( $= \{W_e, \Theta_e, U_e\}^T$ ,  $W_e$  represents the radial,  $\Theta_e$  represents the azimuthal and  $U_e$ , the axial displacement field).  $\lambda$  and  $\mu$  are the Lamé's coefficients,  $\rho_s$  is the density of the tube and  $\nabla$  is the gradient operator in three dimension given by

$$\nabla = \frac{\partial}{\partial r} \mathbf{e}_r + \frac{1}{r} \frac{\partial}{\partial \theta} \mathbf{e}_\theta + \frac{\partial}{\partial z} \mathbf{e}_z. \quad (21)$$

The displacement vector  $\mathbf{U}$  may be represented using the Helmholtz decomposition method as

$$\mathbf{U} = \nabla \phi + \nabla \times \boldsymbol{\psi}, \quad (22)$$

where  $\phi$  is a scalar potential and  $\boldsymbol{\psi}$  is a vector potential. Substituting for  $\mathbf{U}$  in Eq. (20) yields,

$$\begin{aligned} \mu \nabla^2 (\nabla \phi + \nabla \times \boldsymbol{\psi}) + (\lambda + \mu) \nabla \nabla \cdot (\nabla \phi + \nabla \times \boldsymbol{\psi}) \\ = \rho_s \frac{\partial^2}{\partial t^2} (\nabla \phi + \nabla \times \boldsymbol{\psi}). \end{aligned} \quad (23)$$

Rearranging the above equation, the obtained expression is,

$$\begin{aligned} \nabla (\mu \nabla^2 \phi + (\lambda + \mu) \nabla^2 \phi - \rho_s \ddot{\phi}) + \\ \nabla \times (\mu \nabla^2 \boldsymbol{\psi} - \rho_s \ddot{\boldsymbol{\psi}}) = 0. \end{aligned} \quad (24)$$

Eq. (24) may be separated to two equations each corresponding to the scalar and vector potential fields as,

$$(\lambda + 2\mu) \nabla^2 \phi - \rho_s \ddot{\phi} = 0 \quad \text{and} \quad \mu \nabla^2 \boldsymbol{\psi} - \rho_s \ddot{\boldsymbol{\psi}} = 0.$$

The above equations are rearranged as,

$$\nabla^2 \phi = \frac{1}{C_L^2} \ddot{\phi}, \quad (25)$$

where,  $C_L^2 = \frac{\lambda + 2\mu}{\rho_s}$  and

$$\nabla^2 \boldsymbol{\psi} = \frac{1}{C_T^2} \ddot{\boldsymbol{\psi}}, \quad (26)$$

where,  $C_T^2 = \frac{\mu}{\rho_s}$ . Substituting for  $\boldsymbol{\psi} = \psi_r \mathbf{e}_r + \psi_\theta \mathbf{e}_\theta + \psi_z \mathbf{e}_z$  in Eq. (26) results in [16]

$$\nabla^2 \psi_r - \frac{\psi_r}{r^2} - \frac{2}{r^2} \frac{\partial \psi_\theta}{\partial \theta} = \frac{1}{C_T^2} \frac{\partial^2 \psi_r}{\partial t^2}, \quad (27)$$

$$\nabla^2 \psi_\theta - \frac{\psi_\theta}{r^2} - \frac{2}{r^2} \frac{\partial \psi_r}{\partial \theta} = \frac{1}{C_T^2} \frac{\partial^2 \psi_\theta}{\partial t^2}, \quad (28)$$

and

$$\nabla^2 \psi_z = \frac{1}{C_T^2} \frac{\partial^2 \psi_z}{\partial t^2}. \quad (29)$$

The following subsections discuss the solution of the governing differential equations for the scalar potential function (Eq. (25)) and the vector potential functions (Eqs. (27) - (29)).

#### 4.1.1 The scalar potential function $\phi$

A plane wave propagating in the positive  $z$  direction can be written in the form

$$\phi(r, \theta, z, t) = \Phi(r) \Theta(\theta) e^{i(k_z z - \omega t)}. \quad (30)$$

Substituting Eq. (30) in Eq. (25) and simplifying gives,

$$\begin{aligned} \frac{r^2}{\Phi(r)} \frac{\partial^2 \Phi(r)}{\partial r^2} + \frac{r}{\Phi(r)} \frac{\partial \Phi(r)}{\partial r} + r^2 \left( \frac{\omega^2}{C_L^2} - k_z^2 \right) \\ = -\frac{1}{\Theta(\theta)} \frac{\partial^2 \Theta(\theta)}{\partial \theta^2}. \end{aligned} \quad (31)$$

The above equation is satisfied only if both the left and the right hand sides are equal to a constant, say  $n^2$ . Thus, the differential equations governing  $\Phi(r)$  and  $\Theta(\theta)$  can be separated as

$$\frac{\partial^2 \Phi(r)}{\partial r^2} + \frac{1}{r} \frac{\partial \Phi(r)}{\partial r} + \left( \frac{\omega^2}{C_L^2} - k_z^2 - \frac{n^2}{r^2} \right) \Phi(r) = 0 \quad (32)$$

and

$$\frac{\partial^2 \Theta(\theta)}{\partial \theta^2} + n^2 \Theta(\theta) = 0. \quad (33)$$

Eq. (32) can be further simplified to

$$\frac{d^2\Phi}{dr^2} + \frac{1}{r} \frac{d\Phi}{dr} + \left( \beta_1^2 - \frac{n^2}{r^2} \right) \Phi = 0, \quad (34)$$

where  $\beta_1^2 = \frac{\omega^2}{C_L^2} - k_z^2$ . The solution of Eq. (34) is given by

$$\Phi(r) = A_1 J_n(\beta_1 r) + A_2 Y_n(\beta_1 r), \quad (35)$$

where  $J_n$  and  $Y_n$  are the Bessel function of the first and the second kinds of order  $n$  respectively. The solution to Eq. (33) can be derived as,

$$\Theta(\theta) = A_3 \cos(n\theta) + A_4 \sin(n\theta). \quad (36)$$

In Eqs. (35) and (36),  $A_1, A_2, A_3$  and  $A_4$  are the unknown constants. Substituting Eq. (35) and Eq. (36) in to Eq. (30), the scalar potential function is given by

$$\phi(r, \theta, z, t) = [A_1 J_n(\beta_1 r) + A_2 Y_n(\beta_1 r)] \times [A_3 \cos(n\theta) + A_4 \sin(n\theta)] e^{i(k_z z - \omega t)}. \quad (37)$$

#### 4.1.2 The vector potential function $\psi$

It can be observed from Eqs. (27)-(28) that, both  $\psi_r$  and  $\psi_\theta$  are coupled and need to be solved simultaneously. However, Eq (29) can be solved independently for  $\psi_z$ . Let  $\psi_r$  and  $\psi_\theta$  be of the form

$$\psi_r(r, \theta, z, t) = \Psi_r(r) \sin(n\theta) e^{i(k_z z - \omega t)} \quad (38)$$

and

$$\psi_\theta(r, \theta, z, t) = \Psi_\theta(r) \cos(n\theta) e^{i(k_z z - \omega t)}. \quad (39)$$

Substituting Eq. (38) and Eq. (39) in Eq. (27) and Eq. (28), respectively,

$$\begin{aligned} \frac{d^2\Psi_r}{dr^2} + \frac{1}{r} \frac{d\Psi_r}{dr} + \frac{1}{r^2} (-n^2\Psi_r + 2n\Psi_\theta - \Psi_r) \\ - k_z^2\Psi_r + \frac{\omega^2}{C_T^2}\Psi_r = 0 \end{aligned} \quad (40) \quad \text{and}$$

and

$$\begin{aligned} \frac{d^2\Psi_\theta}{dr^2} + \frac{1}{r} \frac{d\Psi_\theta}{dr} + \frac{1}{r^2} (-n^2\Psi_\theta + 2n\Psi_r - \Psi_\theta) \\ - k_z^2\Psi_\theta + \frac{\omega^2}{C_T^2}\Psi_\theta = 0. \end{aligned} \quad (41)$$

Subtracting Eq. (41) from Eq. (40),

$$\begin{aligned} \frac{d^2(\Psi_r - \Psi_\theta)}{dr^2} + \frac{1}{r} \frac{d(\Psi_r - \Psi_\theta)}{dr} \\ + \frac{1}{r^2} \left( -n^2(\Psi_r - \Psi_\theta) + 2n(\Psi_\theta - \Psi_r) - (\Psi_r - \Psi_\theta) \right) \\ - k_z^2(\Psi_r - \Psi_\theta) + \frac{\omega^2}{C_T^2}(\Psi_r - \Psi_\theta) = 0. \end{aligned} \quad (42)$$

Solving,

$$\Psi_r - \Psi_\theta = C_1 J_{n+1}(\beta_2 r) + C_2 Y_{n+1}(\beta_2 r), \quad (43)$$

where  $\beta_2^2 = \frac{\omega^2}{C_T^2} - k_z^2$ ,  $C_1$  and  $C_2$  are unknown constants. Adding Eqs. (40) and (41),

$$\begin{aligned} \frac{d^2(\Psi_r + \Psi_\theta)}{dr^2} + \frac{1}{r} \frac{d(\Psi_r + \Psi_\theta)}{dr} \\ + \frac{1}{r^2} \left( -n^2(\Psi_r + \Psi_\theta) + 2n(\Psi_\theta + \Psi_r) - (\Psi_r + \Psi_\theta) \right) \\ - k_z^2(\Psi_r + \Psi_\theta) + \frac{\omega^2}{C_T^2}(\Psi_r + \Psi_\theta) = 0. \end{aligned} \quad (44)$$

Solving,

$$\Psi_r + \Psi_\theta = D_1 J_{n-1}(\beta_2 r) + D_2 Y_{n-1}(\beta_2 r), \quad (45)$$

where  $D_1$  and  $D_2$  are unknown constants. Using Eq. (43) and Eq. (45),  $\Psi_r$  and  $\Psi_\theta$  can be obtained as

$$\begin{aligned} \Psi_r = C_1 J_{n+1}(\beta_2 r) + C_2 Y_{n+1}(\beta_2 r) \\ + D_1 J_{n-1}(\beta_2 r) + D_2 Y_{n-1}(\beta_2 r) \end{aligned} \quad (46)$$

$$\begin{aligned} \Psi_\theta = D_1 J_{n-1}(\beta_2 r) + D_2 Y_{n-1}(\beta_2 r) \\ - C_1 J_{n+1}(\beta_2 r) - C_2 Y_{n+1}(\beta_2 r). \end{aligned} \quad (47)$$



However, for vector potential function,  $\nabla \cdot \psi = 0$  [16]. This necessitates  $\Psi_r = -\Psi_\theta$ . Therefore, using Eq. (45),  $D1 = D2 = 0$ . Thus,

$$\Psi_r(r) = C_1 J_{n+1}(\beta_2 r) + C_2 Y_{n+1}(\beta_2 r) \quad (48)$$

and

$$\Psi_\theta(\theta) = -C_1 J_{n+1}(\beta_2 r) - C_2 Y_{n+1}(\beta_2 r), \quad (49)$$

Using the above equations, the radial (Eq. (38)) and azimuthal (Eq. (39)) components of the vector potential function are given by

$$\psi_r(r, \theta, z, t) = [C_1 J_{n+1}(\beta_2 r) + C_2 Y_{n+1}(\beta_2 r)] \cdot \sin(n\theta) e^{i(k_z z - \omega t)} \quad (50)$$

and

$$\psi_\theta(r, \theta, z, t) = -[C_1 J_{n+1}(\beta_2 r) + C_2 Y_{n+1}(\beta_2 r)] \cdot \cos(n\theta) e^{i(k_z z - \omega t)}. \quad (51)$$

The solution of the vector potential  $\psi_z$  is similar to the solution of the scalar potential (Eq. (37)) which can be derived as,

$$\psi_z(r, \theta, z, t) = [B_1 J_n(\beta_2 r) + B_2 Y_n(\beta_2 r)] \cdot [B_3 \cos(n\theta) + B_4 \sin(n\theta)] e^{i(k_z z - \omega t)}, \quad (52)$$

The scalar and vector potential functions satisfy the Navier-Lame equation for  $n = 0$  and all positive integer values of  $n$ . Therefore, the complete solution to Navier-Lame equation can be obtained as

$$\phi(r, \theta, z, t) = \sum_{n=0}^{\infty} [A_1 J_n(\beta_1 r) + A_2 Y_n(\beta_1 r)] \cdot [A_3 \cos(n\theta) + A_4 \sin(n\theta)] e^{i(k_z z - \omega t)}, \quad (53)$$

$$\psi_r(r, \theta, z, t) = \sum_{n=0}^{\infty} [C_1 J_{n+1}(\beta_2 r) + C_2 Y_{n+1}(\beta_2 r)] \cdot \sin(n\theta) e^{i(k_z z - \omega t)}, \quad (54)$$

$$\psi_\theta(r, \theta, z, t) = \sum_{n=0}^{\infty} -[C_1 J_{n+1}(\beta_2 r) + C_2 Y_{n+1}(\beta_2 r)] \cdot \cos(n\theta) e^{i(k_z z - \omega t)} \quad (55)$$

and

$$\psi_z(r, \theta, z, t) = \sum_{n=0}^{\infty} [B_1 J_n(\beta_2 r) + B_2 Y_n(\beta_2 r)] \cdot [B_3 \cos(n\theta) + B_4 \sin(n\theta)] e^{i(k_z z - \omega t)} \quad (56)$$

In this work, the above expressions are truncated to only  $n = 0$  and  $n = 1$  terms and further used to compute the elastic tube displacement and stress fields.

#### 4.1.3 Elastic tube displacement components

In this subsection, the displacement components of the elastic tube in radial ( $W_e$ ), azimuthal ( $\Theta_e$ ) and axial ( $U_e$ ) directions, are derived using the potential functions derived in the previous subsection. Using Eq. (22), the displacement components are

$$W_e(r, \theta, z, t) = \frac{\partial \phi}{\partial r} + \frac{1}{r} \frac{\partial \psi_z}{\partial \theta} - \frac{\partial \psi_\theta}{\partial z}, \quad (57)$$

$$\Theta_e(r, \theta, z, t) = \frac{1}{r} \frac{\partial \phi}{\partial \theta} + \frac{\partial \psi_r}{\partial z} - \frac{\partial \psi_z}{\partial r} \quad (58)$$

and

$$U_e(r, \theta, z, t) = \frac{\partial \phi}{\partial z} + \frac{1}{r} \frac{\partial \psi_z}{\partial \theta} - \frac{\partial \psi_\theta}{\partial z} \quad (59)$$

Substituting for the scalar (Eq. (53)) and the vector potential (Eqs. (54) - (56)) functions,

$$\begin{aligned} W_e(r, \theta, z, t) = e^{i(k_z z - \omega t)} & \left\{ \frac{1}{r} [r \beta_1 J_0(r \beta_1) \cos(\theta) \right. \\ & - J_1(r \beta_1)(\cos(\theta) + r \beta_1)] E_1 \\ & + \frac{1}{r} \sin(\theta) [r \beta_1 J_0(r \beta_1) - J_1(r \beta_1)] E_2 \\ & + \frac{1}{r} [r \beta_1 Y_0(r \beta_1) \cos(\theta) - Y_1(r \beta_1)(\cos(\theta) + r \beta_1)] F_1 \\ & + \frac{1}{r} \sin(\theta) [r \beta_1 Y_0(r \beta_1) - Y_1(r \beta_1)] F_2 \\ & \left. + i k_z [J_1(r \beta_2) + J_2(r \beta_2) \cos(\theta)] G_1 \right\} \end{aligned}$$

$$\begin{aligned}
& + ik_z[J_1(r\beta_2) + J_2(r\beta_2)\cos(\theta)]G_2 \\
& + \left[\frac{1}{r}J_1(r\beta_2)\cos(\theta)\right]H_1 + \left[\frac{1}{r}Y_1(r\beta_2)\cos(\theta)\right]H_2 \\
& - \left[\frac{1}{r}J_1(r\beta_2)\sin(\theta)\right]I_1 - \left[\frac{1}{r}Y_1(r\beta_2)\sin(\theta)\right]I_2 \Big\}, \quad (60)
\end{aligned}$$

where,  $E_1, E_2, F_1, F_2, G_1, G_2, H_1, H_2, I_1$  and  $I_2$  are unknown constants with  $E_1 = A_1A_3, E_2 = A_1A_4, F_1 = A_2A_3, F_2 = A_2A_4, G_1 = C_1, G_2 = C_2, H_1 = B_1B_4, H_2 = B_2B_4, I_1 = B_1B_3$  and  $I_2 = B_2B_3$ ,

$$\begin{aligned}
\Theta_e(r, \theta, z, t) = e^{i(k_z z - \omega t)} & \left\{ \frac{-1}{r}[J_1(r\beta_1)\sin(\theta)]E_1 \right. \\
& + \frac{1}{r}[J_1(r\beta_1)\cos(\theta)]E_2 + \frac{-1}{r}[Y_1(r\beta_1)\sin(\theta)]F_1 \\
& + \frac{1}{r}[Y_1(r\beta_1)\cos(\theta)]F_2 + [ik_z J_2(r\beta_2)\sin(\theta)]G_1 \\
& + [ik_z Y_2(r\beta_2)\sin(\theta)]G_2 \\
& - \frac{\beta_2 \sin(\theta)}{2}[J_0(r\beta_2) - J_2(r\beta_2)]H_1 \\
& - \frac{\beta_2 \sin(\theta)}{2}[Y_0(r\beta_2) - Y_2(r\beta_2)]H_2 \\
& + \frac{1}{r}\{-r\beta_2 J_0(r\beta_2)\cos(\theta) + J_1(r\beta_2)[r\beta_2 + \cos(\theta)]\}I_1 \\
& \left. + \frac{1}{r}\{-r\beta_2 Y_0(r\beta_2)\cos(\theta) + Y_1(r\beta_2)[r\beta_2 + \cos(\theta)]\}I_2 \right\} \quad (61)
\end{aligned}$$

and

$$\begin{aligned}
U_e(r, \theta, z, t) & = e^{i(k_z z - \omega t)} \left\{ ik_z[J_0(r\beta_1) + J_1(r\beta_1)\cos(\theta)]E_1 \right. \\
& + [ik_z J_1(r\beta_1)\sin(\theta)]E_2 + ik_z[Y_0(r\beta_1) + Y_1(r\beta_1)\cos(\theta)]F_1 \\
& + [ik_z Y_1(r\beta_1)\sin(\theta)]F_2 - \beta_2[J_0(r\beta_2) + J_1(r\beta_2)\cos(\theta)]G_1 \\
& \left. - \beta_2[Y_0(r\beta_2) + Y_1(r\beta_2)\cos(\theta)]G_2 \right\}. \quad (62)
\end{aligned}$$

The spatio-temporal  $(r, \theta, z, t)$  displacement is then transformed to the wavenumber-frequency  $(r, \theta, k_z, \omega)$  domain using the Fourier transform pairs,

$$\begin{aligned}
\hat{G}(r, \theta, k_z, \omega) & = \frac{1}{4\pi^2} \int_{-\infty}^{\infty} \int_{-\infty}^{\infty} g(r, \theta, z, t) e^{-i(k_z z - \omega t)} dz dt, \quad (63)
\end{aligned}$$

and

$$\begin{aligned}
g(r, \theta, z, t) & = \int_{-\infty}^{\infty} \int_{-\infty}^{\infty} \hat{G}(r, \theta, k_z, \omega) e^{i(k_z z - \omega t)} dk_z d\omega. \quad (64)
\end{aligned}$$

The transformed displacement components are given below,

i Radial displacement,

$$\begin{aligned}
\hat{W}_e(r, \theta, k_z, \omega) = & \left\{ \frac{-\chi_1}{2} \{2J_1(r\beta_1) + [J_2(r\beta_1) \right. \\
& - J_0(r\beta_1)]\cos(\theta)\} \Big\} \hat{P}_1(k_z, \omega) \\
& + \left\{ \frac{\chi_1}{2} [J_0(r\beta_1) - J_2(r\beta_1)]\sin(\theta) \right\} \hat{P}_2(k_z, \omega) \\
& + \left\{ \frac{-\chi_1}{2} \{2Y_1(r\beta_1) + [Y_2(r\beta_1) \right. \\
& - Y_0(r\beta_1)]\cos(\theta)\} \Big\} \hat{Q}_1(k_z, \omega) \\
& + \left\{ \frac{\chi_1}{2} [Y_0(r\beta_1) - Y_2(r\beta_1)]\sin(\theta) \right\} \hat{Q}_2(k_z, \omega) \\
& - \left\{ \chi_2 [J_1(r\beta_2) + J_2(r\beta_2)\cos(\theta)] \right\} \hat{R}_1(k_z, \omega) \\
& - \left\{ \chi_2 [Y_1(r\beta_2) + Y_2(r\beta_2)\cos(\theta)] \right\} \hat{R}_2(k_z, \omega) \\
& + \left\{ \frac{1}{r} [J_1(r\beta_2)\cos(\theta)] \right\} \hat{S}_1(k_z, \omega) \\
& + \left\{ \frac{1}{r} [Y_1(r\beta_2)\cos(\theta)] \right\} \hat{S}_2(k_z, \omega) \\
& + \left\{ \frac{1}{r} [J_1(r\beta_2)\sin(\theta)] \right\} \hat{T}_1(k_z, \omega) \\
& + \left\{ \frac{1}{r} [Y_1(r\beta_2)\sin(\theta)] \right\} \hat{T}_2(k_z, \omega), \quad (65)
\end{aligned}$$

where  $\hat{P}_1(k_z, \omega), \hat{P}_2(k_z, \omega), \hat{Q}_1(k_z, \omega), \hat{Q}_2(k_z, \omega), \hat{R}_1(k_z, \omega), \hat{R}_2(k_z, \omega), \hat{S}_1(k_z, \omega), \hat{S}_2(k_z, \omega), \hat{T}_1(k_z, \omega)$  and  $\hat{T}_2(k_z, \omega)$  are the unknown variables and  $\chi_1 = \frac{\beta_1}{jk_z}$  and  $\chi_2 = \frac{jk_z}{\beta_2}$ .

ii Azimuthal displacement,

$$\begin{aligned}
\hat{\Theta}_e(r, \theta, k_z, \omega) = & \left\{ \frac{-\chi_1}{r\beta_1} [J_1(r\beta_1) \sin(\theta)] \right\} \hat{P}_1(k_z, \omega) \\
& + \left\{ \frac{\chi_1}{r\beta_1} [J_1(r\beta_1) \cos(\theta)] \right\} \hat{P}_2(k_z, \omega) \\
& + \left\{ \frac{-\chi_1}{r\beta_1} [Y_1(r\beta_1) \sin(\theta)] \right\} \hat{Q}_1(k_z, \omega) \\
& + \left\{ \frac{\chi_1}{r\beta_1} [Y_1(r\beta_1) \cos(\theta)] \right\} \hat{Q}_2(k_z, \omega) \\
& - \left\{ \chi_2 J_2(r\beta_2) \sin(\theta) \right\} \hat{R}_1(k_z, \omega) \\
& - \left\{ \chi_2 Y_2(r\beta_2) \sin(\theta) \right\} \hat{R}_2(k_z, \omega) \\
& + \left\{ \frac{\sin(\theta)}{r} [J_1(r\beta_2) - r\beta_2 J_0(r\beta_2)] \right\} \hat{S}_1(k_z, \omega) \\
& + \left\{ \frac{\sin(\theta)}{r} [Y_1(r\beta_2) - r\beta_2 Y_0(r\beta_2)] \right\} \hat{S}_2(k_z, \omega) \\
& + \left\{ \beta_2 J_0(r\beta_2) \cos(\theta) \right. \\
& \left. - \frac{1}{r} \{ J_1(r\beta_2) * [r\beta_2 + \cos(\theta)] \} \right\} \hat{T}_1(k_z, \omega) \\
& + \left\{ \beta_2 Y_0(r\beta_2) \cos(\theta) \right. \\
& \left. - \frac{1}{r} \{ Y_1(r\beta_2) * [r\beta_2 + \cos(\theta)] \} \right\} \hat{T}_2(k_z, \omega) \quad (66)
\end{aligned}$$

and

iii Axial displacement,

$$\begin{aligned}
\hat{U}_e(r, \theta, k_z, \omega) = & \left\{ J_0(r\beta_1) + J_1(r\beta_1) \cos(\theta) \right\} \hat{P}_1(k_z, \omega) \\
& + \left\{ J_1(r\beta_1) \sin(\theta) \right\} \hat{P}_2(k_z, \omega) \\
& + \left\{ Y_0(r\beta_1) + Y_1(r\beta_1) \cos(\theta) \right\} \hat{Q}_1(k_z, \omega) \\
& + \left\{ Y_1(r\beta_1) \sin(\theta) \right\} \hat{Q}_2(k_z, \omega)
\end{aligned}$$

$$\begin{aligned}
& + \left\{ J_0(r\beta_2) + J_1(r\beta_2) \cos(\theta) \right\} \hat{R}_1(k_z, \omega) \\
& + \left\{ Y_0(r\beta_2) + Y_1(r\beta_2) \cos(\theta) \right\} \hat{R}_2(k_z, \omega). \quad (67)
\end{aligned}$$

The unknown variables in the displacement components, are related to the unknown constants  $A_1, A_2, A_3, A_4, B_1, B_2, B_3, B_4, C_1$  and  $C_2$  in the potential functions as,

$$\hat{P}_1(k_z, \omega) = 2\pi i A_1 A_3 k_z \delta(k + k_z) \delta(\omega - \omega_0), \quad (68)$$

$$\hat{P}_2(k_z, \omega) = 2\pi i A_2 A_3 k_z \delta(k + k_z) \delta(\omega - \omega_0), \quad (69)$$

$$\hat{Q}_1(k_z, \omega) = 2\pi i A_1 A_4 k_z \delta(k + k_z) \delta(\omega - \omega_0), \quad (70)$$

$$\hat{Q}_2(k_z, \omega) = 2\pi i A_2 A_4 k_z \delta(k + k_z) \delta(\omega - \omega_0), \quad (71)$$

$$\hat{R}_1(k_z, \omega) = -2\pi C_1 \beta_1 \delta(k + k_z) \delta(\omega - \omega_0), \quad (72)$$

$$\hat{R}_2(k_z, \omega) = -2\pi C_2 \beta_1 \delta(k + k_z) \delta(\omega - \omega_0), \quad (73)$$

$$\hat{S}_1(k_z, \omega) = 2\pi B_1 B_4 \delta(k + k_z) \delta(\omega - \omega_0), \quad (74)$$

$$\hat{S}_2(k_z, \omega) = 2\pi B_2 B_4 \delta(k + k_z) \delta(\omega - \omega_0), \quad (75)$$

$$\hat{T}_1(k_z, \omega) = -2\pi B_1 B_3 \delta(k + k_z) \delta(\omega - \omega_0), \quad (76)$$

$$\hat{T}_2(k_z, \omega) = -2\pi B_2 B_3 \delta(k + k_z) \delta(\omega - \omega_0), \quad (77)$$

where  $\delta$  is the dirac delta function. From the above equations (Eqs. (68)-(77)), two unknown variables can be expressed in terms of other variables as,

$$\begin{aligned}
\hat{Q}_2(k_z, \omega) &= \frac{\hat{P}_2(k_z, \omega) \hat{Q}_1(k_z, \omega)}{\hat{P}_1(k_z, \omega)}, \\
\hat{T}_2(k_z, \omega) &= \frac{\hat{S}_2(k_z, \omega) \hat{T}_1(k_z, \omega)}{\hat{S}_1(k_z, \omega)}. \quad (78)
\end{aligned}$$

From the displacement components derived in this section, there are ten unknown variables, out of which only eight are independent (Eq. (78)). Further, using the displacement components, normal and shear stresses are derived which is discussed in next section.

#### 4.1.4 Elastic stress components

The elastic tube and the acoustic fluid inside the tube are coupled through displacement and stress boundary conditions. Of all the stress components, only  $\tau_{rr}$ ,  $\tau_{r\theta}$ ,  $\tau_{rz}$ , and  $\tau_{z\theta}$  are of interest to us. These components may be computed using the constitutive relations [15]. They are,

$$\tau_{rr}(r, \theta, z, t) = (\lambda + 2\mu) \frac{\partial W_e}{\partial r} + \frac{\lambda}{r} \left( W_e + \frac{\partial \Theta_e}{\partial \theta} \right) + \lambda \frac{\partial U_e}{\partial z}, \quad (79)$$

$$\tau_{rz}(r, \theta, z, t) = \mu \left( \frac{\partial W_e}{\partial z} + \frac{\partial U_e}{\partial r} \right), \quad (80)$$

$$\tau_{r\theta}(r, \theta, z, t) = \mu \left( \frac{1}{r} \frac{\partial W_e}{\partial \theta} + \frac{\partial \Theta_e}{\partial r} - \frac{\Theta_e}{r} \right), \quad (81)$$

and

$$\tau_{z\theta}(r, \theta, z, t) = \mu \left( \frac{\partial \Theta_e}{\partial z} + \frac{1}{r} \frac{\partial U_e}{\partial \theta} \right). \quad (82)$$

The above constitutive relations are transformed into the frequency - wavenumber ( $\omega - k_z$ ) domain using the Fourier transform pair (Eqs. (63) and (64)). Further, displacement components derived in the previous subsection are substituted to obtain a closed form expressions for these stress components (see Eqs. (??), (??), (??) and (??)). A detailed derivation of the stress components using the constitutive relations are given in ??

#### 4.2 The interior fluid acoustic pressure and displacement fields

The interior fluid is assumed to be confined inside an infinitely long elastic tube. The acoustic wave propagation in the fluid is governed by

$$\nabla^2 p_f(r, \theta, z, t) = \frac{1}{c_a^2} \frac{\partial^2 p_f(r, \theta, z, t)}{\partial t^2}, \quad (83)$$

where  $p_f$  is the acoustic pressure,  $c_a$  is the speed of sound in the fluid inside the tube and  $\nabla^2$  is the Laplacian. In

cylindrical coordinates,

$$\nabla^2 = \frac{\partial^2}{\partial r^2} + \frac{1}{r} \frac{\partial}{\partial r} + \frac{1}{r^2} \frac{\partial^2}{\partial \theta^2} + \frac{\partial^2}{\partial z^2}. \quad (84)$$

Assuming a plane wave propagation in the  $z$  direction and using variable separable form for  $p_f$ ,

$$p_f(r, \theta, z, t) = R(r)\Theta(\theta)e^{j(k_z z - \omega t)}. \quad (85)$$

Substituting Eq. (85) in Eq. (83), and rearranging gives

$$\frac{r^2}{R} \frac{\partial^2 R(r)}{\partial r^2} + \frac{r}{R} \frac{\partial R(r)}{\partial r} + \alpha^2 r^2 = -\frac{1}{\Theta} \frac{\partial^2 \Theta}{\partial \theta^2}, \quad (86)$$

where  $\alpha^2 = \frac{\omega^2}{c_a^2} - k_z^2$ . Only those solutions are valid for which the left hand side and the right hand sides of the above equation are equal to a positive constant ( $n^2$ ). Therefore,

$$\frac{r^2}{R} \frac{\partial^2 R(r)}{\partial r^2} + \frac{r}{R} \frac{\partial R(r)}{\partial r} + \alpha^2 r^2 = -\frac{1}{\Theta} \frac{\partial^2 \Theta}{\partial \theta^2} = n^2. \quad (87)$$

From the above equation,  $\Theta(\theta)$  can be obtained by solving

$$\frac{\partial^2 \Theta}{\partial \theta^2} + n^2 \Theta = 0. \quad (88)$$

A general solution to Eq. (88) is,

$$\Theta(\theta) = P_{f01} \cos(n\theta) + P_{f02} \sin(n\theta), \quad (89)$$

where  $P_{f01}$  and  $P_{f02}$  are unknowns. Similarly from Eq. (87),  $R(r)$  is governed by,

$$\frac{\partial^2 R}{\partial r^2} + \frac{1}{r} \frac{\partial R}{\partial r} + \left( \alpha^2 - \frac{n^2}{r^2} \right) R = 0. \quad (90)$$

The solution to Eq. (90) is

$$R(r) = P_{f03} J_n(\alpha r) + P_{f04} Y_n(\alpha r), \quad (91)$$

where  $P_{f03}$  and  $P_{f04}$  are unknowns. As  $r \rightarrow 0$ ,  $Y_n(\alpha r) \rightarrow -\infty$ , the second term on the right hand

side must vanish for all valid pressure fields. Therefore,  $P_{f04} = 0$ . Thus, using Eqs. (85), (89) and (91),

$$p_f(r, \theta, z, t) = P_{f03} J_n(\alpha r) [P_{f01} \cos(n\theta) + P_{f02} \sin(n\theta)] e^{j(k_z z - \omega t)} \quad (92)$$

The above equation is valid for  $n = 0, 1, 2, \dots$  etc. The complete solution to the acoustic pressure field may be written as,

$$p_f(r, \theta, z, t) = \sum_{n=0}^{\infty} P_{f03} J_n(\alpha r) [P_{f01} \cos(n\theta) + P_{f02} \sin(n\theta)] e^{j(k_z z - \omega t)} \quad (93)$$

Only  $n = 0$  and  $n = 1$  terms in Eq. (93) are considered in this work. Further, Eq. (93) is transformed to the frequency-wavenumber ( $\omega - k_z$ ) domain using Eq. (63) and is given by

$$\hat{p}_f(r, \theta, k_z, \omega) = \hat{P}_{f1}(k_z, \omega) [J_0(\alpha r) + J_1(\alpha r) \cos(\theta)] + \hat{P}_{f2}(k_z, \omega) J_1(\alpha r) \sin(\theta), \quad (94)$$

where  $\hat{P}_{f1}(k_z, \omega)$  and  $\hat{P}_{f2}(k_z, \omega)$  are two unknowns, which are function of the constants  $P_{f01}$ ,  $P_{f02}$  and  $P_{f03}$ . They are related as,

$$\hat{P}_{f1}(k_z, \omega) = 2\pi P_{f03} P_{f01} \delta(k + k_z) \delta(\omega - \omega_0) \quad (95)$$

and

$$\hat{P}_{f2}(k_z, \omega) = 2\pi P_{f03} P_{f02} \delta(k + k_z) \delta(\omega - \omega_0). \quad (96)$$

The acoustic particle velocity in the radial, azimuthal and axial directions can be obtained with the help of Euler equation,

$$\nabla p_f(r, \theta, z, t) = -\rho \frac{\partial \mathbf{u}_f(r, \theta, z, t)}{\partial t}, \quad (97)$$

where  $\nabla$  is the gradient operator and  $\mathbf{u}_f$  is the acoustic particle velocity. The acoustic fluid particle velocity  $\mathbf{u}_f$  may be represented as,

$$\mathbf{u}_f(r, \theta, z, t) = u_{fr}(r, \theta, z, t) \mathbf{e}_r + u_{f\theta}(r, \theta, z, t) \mathbf{e}_\theta$$

$$+ u_{fz}(r, \theta, z, t) \mathbf{e}_z, \quad (98)$$

where  $u_{fr}$ ,  $u_{f\theta}$  and  $u_{fz}$  are the radial, azimuthal and axial components of the fluid particle velocity respectively. In the above equation, as for the acoustic pressure, a harmonic variation in the form of  $e^{j(k_z z - \omega t)}$  is assumed for the particle velocity. Substituting for  $\mathbf{u}_f$  (Eq. (98)) and transforming to the frequency-wavenumber domain, Eq. (97) results

$$\begin{aligned} \frac{\partial \hat{p}_f(r, \theta, k_z, \omega)}{\partial r} \mathbf{e}_r + \frac{1}{r} \frac{\partial \hat{p}_f(r, \theta, k_z, \omega)}{\partial \theta} \mathbf{e}_\theta \\ + \frac{\partial \hat{p}_f(r, \theta, k_z, \omega)}{\partial z} \mathbf{e}_z = j\rho\omega \hat{u}_{fr}(r, \theta, k_z, \omega) \mathbf{e}_r \\ + j\rho\omega \hat{u}_{f\theta}(r, \theta, k_z, \omega) \mathbf{e}_\theta + j\rho\omega \hat{u}_{fz}(r, \theta, k_z, \omega) \mathbf{e}_z. \end{aligned} \quad (99)$$

#### 4.2.1 Radial component of the fluid particle displacement

Comparing and equating the radial components on the left and right hand side of Eq. (99) results in

$$\frac{\partial \hat{p}_f(r, \theta, k_z, \omega)}{\partial r} = j\rho\omega \hat{u}_{fr}(r, \theta, k_z, \omega) \quad (100)$$

Substituting for the acoustic pressure  $\hat{p}_f(r, \theta, k_z, \omega)$  from Eq. (94) and simplifying yields

$$\begin{aligned} \hat{u}_{fr}(r, \theta, k_z, \omega) = \frac{1}{j\rho\omega} \left\{ \alpha J_0(r\alpha) \cos(\theta) \right. \\ \left. - \frac{J_1(r\alpha)}{r} [r\alpha + \cos(\theta)] \right\} \hat{P}_{f1} \\ + \frac{1}{j\rho\omega} \left\{ \frac{\alpha \sin(\theta)}{2} [J_0(r\alpha) - J_2(r\alpha)] \right\} \hat{P}_{f2}. \end{aligned} \quad (101)$$

Let  $U_{fr}$  be the radial displacement of the fluid particle, defined by

$$U_{fr}(r, \theta, z, t) = \tilde{U}_{fr}(r, \theta) e^{j(k_z z - \omega t)}. \quad (102)$$

In the frequency-wavenumber domain, the fluid particle displacement and velocity in the radial directions are related as

$$\hat{U}_{fr}(r, \theta, k_z, \omega) = \frac{j}{\omega} \hat{u}_{fr}(r, \theta, k_z, \omega). \quad (103)$$

Substituting for  $\hat{u}_{fr}(r, \theta, k_z, \omega)$  (Eq. (101)) in the above equation, the radial component of the fluid particle displacement is given by

$$\begin{aligned} \hat{U}_{fr}(r, \theta, k_z, \omega) = & \left\{ \frac{1}{r\rho\omega^2} \{ r\alpha J_0(r\alpha) \cos(\theta) \right. \\ & \left. - J_1(r\alpha) [r\alpha + \cos(\theta)] \} \right\} \hat{P}_{f1} \\ & + \left\{ \frac{\sin(\theta)}{r\rho\omega^2} [r\alpha J_0(r\alpha) - J_1(r\alpha)] \right\} \hat{P}_{f2}. \end{aligned} \quad (104)$$

#### 4.2.2 Azimuthal component of the fluid particle displacement

Comparing and equating the azimuthal components on the left and right hand side of Eq. (99) results in

$$\frac{1}{r} \frac{\partial \hat{p}_f(r, \theta, k_z, \omega)}{\partial \theta} = j\rho\omega \hat{u}_{f\theta}(r, \theta, k_z, \omega) \quad (105)$$

Substituting for the acoustic pressure  $\hat{p}_f(r, \theta, k_z, \omega)$  from Eq. (94) and simplifying yields

$$\begin{aligned} \hat{u}_{f\theta}(r, \theta, k_z, \omega) = & \left\{ \frac{1}{r\rho\omega} [j \sin(\theta) J_1(r\alpha)] \right\} \hat{P}_{f1} \\ & + \left\{ \frac{-1}{r\rho\omega} [j \cos(\theta) J_1(r\alpha)] \right\} \hat{P}_{f2}. \end{aligned} \quad (106)$$

Let  $U_{f\theta}$  be the azimuthal displacement of the fluid particle defined by

$$U_{f\theta}(r, \theta, z, t) = \tilde{U}_{f\theta}(r, \theta) e^{j(k_z z - \omega t)}. \quad (107)$$

In the frequency-wavenumber domain, the fluid particle displacement and velocity in the azimuthal directions are related as

$$\hat{U}_{f\theta}(r, \theta, k_z, \omega) = \frac{j}{\omega} \hat{u}_{f\theta}(r, \theta, k_z, \omega). \quad (108)$$

Substituting for  $\hat{u}_{f\theta}(r, \theta, k_z, \omega)$  (Eq. (106)) in the above equation, the azimuthal component of the fluid particle displacement is given by

$$\begin{aligned} \hat{U}_{f\theta}(r, \theta, k_z, \omega) = & \left\{ \frac{-1}{r\rho\omega^2} [J_1(r\alpha) \sin(\theta)] \right\} \hat{P}_{f1} \\ & + \left\{ \frac{1}{r\rho\omega^2} [J_1(r\alpha) \cos(\theta)] \right\} \hat{P}_{f2} \end{aligned} \quad (109)$$

### 4.3 Boundary conditions

The field variables derived in the previous subsections involve unknown variables. It is shown in section. 4.1 that the elastic tube displacement (Eqs. (65), (66) and (67)) and stress (Eqs. (79), (80), (81) and (82)) fields have eight unknowns:  $\hat{P}_1$ ,  $\hat{P}_2$ ,  $\hat{Q}_1$ ,  $\hat{R}_1$ ,  $\hat{R}_2$ ,  $\hat{S}_1$ ,  $\hat{S}_2$  and  $\hat{T}_1$ . Section. 4.2 shows that the interior fluid pressure (Eq. (94)) and the fluid particle displacement fields (Eqs. (104) and (109)) have two unknowns:  $\hat{P}_{f1}$  and  $\hat{P}_{f2}$ . These ten unknown variables may be computed with the help of boundary conditions at the inner ( $r = a$ ) and the outer ( $r = b$ ) surfaces of the elastic tube. This subsection discusses the ten boundary conditions that are used to compute the ten unknown variables. Note that, in the previous subsection, all the field variables are expressed in  $r - \theta - k_z - \omega$  domain. These closed form expressions are transformed numerically to the  $r - k_\theta - k_z - \omega$  domain using the discrete Fourier transform pair given below before using in the boundary conditions.

$$\hat{G}(r, k_\theta, k_z, \omega) = \sum_{\theta=0}^{N-1} g(r, \theta, k_z, \omega) e^{-j2\pi k_\theta \theta / N} \quad (110)$$

$$g(r, \theta, k_z, \omega) = \frac{1}{N} \sum_{k_\theta=0}^{N-1} \hat{G}(r, k_\theta, k_z, \omega) e^{j2\pi k_\theta \theta / N} \quad (111)$$

The boundary conditions are given below.

1. At the interior surface of the elastic tube ( $r = a$ ), the radial component of the normal stress  $\tau_{rr}$  is equal to the negative of the acoustic pressure  $p_f$ . In the  $k_\theta - k_z - \omega$  domain, this may be written as

$$\hat{\tau}_{rr}(a, k_\theta, k_z, \omega) = -\hat{p}_f(a, k_\theta, k_z, \omega) \quad (112)$$

2. At the exterior surface of the elastic tube ( $r = b$ ), the radial component of the normal stress  $\tau_{rr}$  is equal to the negative of the external turbulent pressure  $p_0$ . In the  $k_\theta - k_z - \omega$  domain, this may be written as

$$\hat{\tau}_{rr}(b, k_\theta, k_z, \omega) = -\hat{p}_0(k_z, \omega) \quad (113)$$

where  $\hat{p}_0(k_z, \omega)$  is assumed to be a function of  $k_z$  and  $\omega$  alone and is given by Eq. (18) for the hybrid model.

3. The exterior and interior surfaces of the elastic tube is assumed to be shear-free. Therefore  $\tau_{rz}|_{r=a,b} = 0$ ,  $\tau_{r\theta}|_{r=a,b} = 0$  and  $\tau_{z\theta}|_{r=a,b} = 0$ . In the  $k_\theta - k_z - \omega$  domain, this may be written as

$$\hat{\tau}_{rz}(r = a, k_\theta, k_z, \omega) = 0, \quad (114)$$

$$\hat{\tau}_{rz}(r = b, k_\theta, k_z, \omega) = 0, \quad (115)$$

$$\hat{\tau}_{r\theta}(r = a, k_\theta, k_z, \omega) = 0, \quad (116)$$

$$\hat{\tau}_{r\theta}(r = b, k_\theta, k_z, \omega) = 0, \quad (117)$$

$$\hat{\tau}_{z\theta}(r = a, k_\theta, k_z, \omega) = 0, \quad (118)$$

and

$$\hat{\tau}_{z\theta}(r = b, k_\theta, k_z, \omega) = 0. \quad (119)$$

4. The radial ( $W_e$ ) and azimuthal ( $\Theta_e$ ) components of the elastic tube displacements at the interior surface ( $r = a$ ) must be equal to respective fluid particle displacement ( $U_{fr}$  and  $U_{f\theta}$ ) at  $r = a$ . In the  $k_\theta - k_z - \omega$  domain, this may be written as

$$\hat{U}_{fr}(a, k_\theta, k_z, \omega) = \hat{W}_e(a, k_\theta, k_z, \omega) \quad (120)$$

and

$$\hat{U}_{f\theta}(a, k_\theta, k_z, \omega) = \hat{\Theta}_e(a, k_\theta, k_z, \omega). \quad (121)$$

The expressions for the acoustic pressure, the fluid and the elastic tube displacement components and the elastic tube stress components derived in the previous subsections are substituted in the above boundary conditions. The resulting equations are given in detail in ??.

#### 4.4 Solution methodology

Previous section discussed the boundary conditions associated with the elastic tube displacements and the acoustic pressure variations inside and outside the elastic tube. These boundary conditions result in ten equations involving twelve unknown variables (see ??). Of the twelve unknown variables, only ten are independent. A further simplification of the boundary condition to include only the ten independent unknowns are presented in ??. The resulting system of algebraic equations may be represented in a matrix form,

$$\mathbf{A}(r, k_\theta, k_z, \omega) \mathbf{x} = \mathbf{b}(r, k_\theta, k_z, \omega), \quad (122)$$

where  $\mathbf{A}$  is the coefficient matrix of order  $10 \times 10$ ,  $\mathbf{x}$  is the unknown variable vector of order  $10 \times 1$  and  $\mathbf{b}$  is the constant vector of order  $10 \times 1$ . A detailed representation of  $\mathbf{A}$ ,  $\mathbf{x}$  and  $\mathbf{b}$  are given in ??. Eq. (122) is solved numerically for the unknown variable vector  $\mathbf{x}$  and the solution is used to compute the interior acoustic pressure field  $\hat{p}_f(r, k_\theta, k_z, \omega)$ . The acoustic pressure field  $\hat{p}_f(r, k_\theta, k_z, \omega)$  is further used to compute (a) azimuthal variation in the acoustic pressure field inside the elastic tube, (b) on-axis flow noise spectrum and (c) on-axis flow noise.

##### 4.4.1 Azimuthal variation in the interior acoustic pressure field

This section describes the method to compute the variation in the acoustic pressure field at the interior surface of the fluid-filled elastic tube. The interior acoustic pressure field  $\hat{p}_f(r, k_\theta, k_z, \omega)$  is first multiplied with the square of the hydrophone response function  $H(k_z)$  (Eq. (11)) and then integrated over the whole wavenumbers to get

$$Q(r = a, k_\theta, f) = 4\pi \int_{-\infty}^{\infty} \hat{p}_f(r = a, \theta, k_z, \omega) |H(k_z)|^2 dk_z. \quad (123)$$

The factor  $4\pi$  is used to account for the negative frequency and radian frequency measure [8] [9] [12]. The azimuthal variation in  $Q(r = a, k_\theta, f)$  may be computed using the inverse Fourier transform,

$$Q(r = a, \theta, f) = \frac{1}{N} \sum_{k_\theta=0}^{N-1} Q(r = a, k_\theta, f) e^{j2\pi k_\theta \theta / N}. \quad (124)$$



The azimuthal variation in acoustic pressure is computed using

$$SPL(r = a, \theta, f) = 10 \log_{10} \left( \frac{|Q(a, \theta, f)|}{p_{ref}^2} \right), \quad (125)$$

at the tube inner surface, where  $p_{ref} = 1\mu Pa$  is the reference acoustic pressure in water.

#### 4.4.2 On-axis flow noise spectrum

This section discusses the estimation of on-axis flow noise spectrum of a fluid-filled elastic tube. Here, the acoustic pressure field  $\hat{p}_f(r, k_\theta, k_z, \omega)$  is integrated over the azimuthal wavenumbers to get the on-axis flow noise spectrum as a function of frequency ( $\omega$ ) and axial wavenumber ( $k_z$ ).

$$\hat{p}_f(r = 0, k_z, \omega) = \int_{-\infty}^{\infty} \hat{p}_f(r = 0, k_\theta, k_z, \omega) dk_\theta. \quad (126)$$

The on-axis flow noise spectrum level can be calculated by

$$SPL(r = 0, k_z, \omega) = 10 \log_{10} \left( \frac{|\hat{p}_f(r = 0, k_z, \omega)|}{p_{ref}^2} \right). \quad (127)$$

#### 4.4.3 On-axis flow noise

This section describes the estimation of on-axis flow noise inside a fluid-filled elastic tube. First the on-axis flow noise spectrum is computed using Eq. (126). It is further multiplied with the square of the hydrophone response function  $H(k_z)$  (Eq. (11)) and integrated over the axial wavenumbers to obtain on-axis flow noise  $Q(r = 0, f)$ ,

$$Q(r = 0, f) = 4\pi \int_{-\infty}^{\infty} \hat{p}_f(r = 0, k_z, \omega) |H(k_z)|^2 dk_z. \quad (128)$$

The on-axis flow noise level can be computed using

$$SPL(r = 0, f) = 10 \log_{10} \left( \frac{|Q(r = 0, f)|}{p_{ref}^2} \right). \quad (129)$$

## 5 RESULTS AND DISCUSSIONS

This work focuses on developing a three-dimensional vibroacoustic model (3D-VA model) to find the flow noise

inside a fluid-filled elastic tube. Previous sections discussed the development of the fully coupled vibroacoustic model, the method for solving the governing differential equation, and the approach for determining the flow noise.

In this section, 3D-VA model is used to estimate the interior acoustic pressure field and the flow noise. Section. 5.1 presents the interior acoustic pressure field for azimuthally varying external pressure excitation over the fluid-filled elastic tube. Section. 5.2 discusses the on-axis flow noise spectrum due to an external turbulent pressure excitation. The external turbulent pressure excitation is computed using the hybrid model (see Section. 3) developed in this work. The results are then compared with those obtained using the tube transfer function [9] and the axisymmetric vibroacoustic [11] [17] models available in the literature. Section. 5.3 presents the on-axis flow noise computed using the 3D-VA model and further compares the results with those predicted using tube transfer function [9] and the axisymmetric [11] models. Further, Section. 5.4 discusses the flow noise variation for various elastic tube diameters at different tow speeds.

### 5.1 Interior acoustic pressure field for azimuthally varying external excitation

The developed 3D-VA model of the fluid-filled elastic tube is initially tested with an exterior harmonic pressure excitation that has a known azimuthal variation. Results for two different external pressure excitation ( $\hat{p}_0(\theta, k_z)$ ) are presented here : (a)  $\hat{p}_0(\theta, k_z) = \sin(\theta)$  (see Fig. 6) and (b)  $\hat{p}_0(\theta, k_z) = \cos(\theta)$  (see Fig. 7).

Figs. 6(a) and 7(a) shows the resulting acoustic pressure variation (see Eqs. (123), (124) and (125) with  $\hat{p}_f$  being replaced with  $\hat{p}_0$ ) along the outer surface. Figs. 6(b) - 6(d) and Figs. 7(b) - 7(d) depicts the azimuthal variation in the acoustic pressure (see Eqs. (123), (124) and (125)) along the tube inner surface at 10 Hz, 100 Hz and 1000 Hz for the two azimuthally different excitations. The Figs. 6 and 7 confirms that the 3D-VA model accurately captures the azimuthal variation (restricted to  $n = 0$  and  $n = 1$ ) in the external pressure excitation.

### 5.2 On-axis acoustic pressure spectrum for external turbulent pressure excitation

This section presents on-axis flow noise spectrum when the elastic tube is excited by the external turbulent pressure field. The external turbulent pressure field (see Fig. 8) is computed using the present hybrid model (Eq. (18)). Further, the present 3D-VA model is used to compute the on-axis flow noise spectrum (see Eqs. 126 and 127). This flow noise spectrum is compared with that

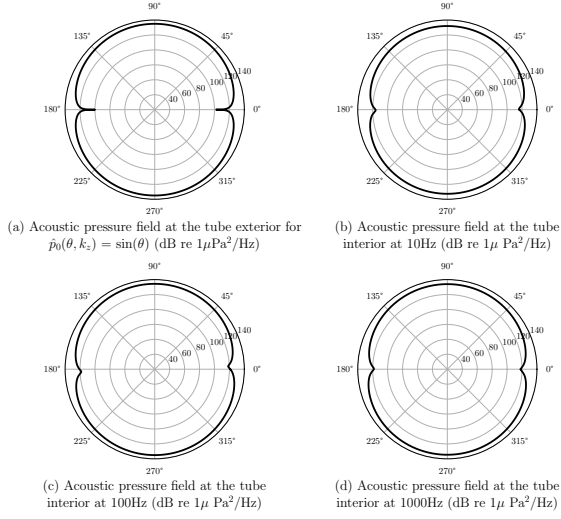


Fig. 6. (a) External acoustic pressure field  $\hat{p}_0(\theta, k_z) = \sin(\theta)$ , (b)-(d) Acoustic pressure field at the inner surface of the tube ( $r = a$ ) for different frequencies.

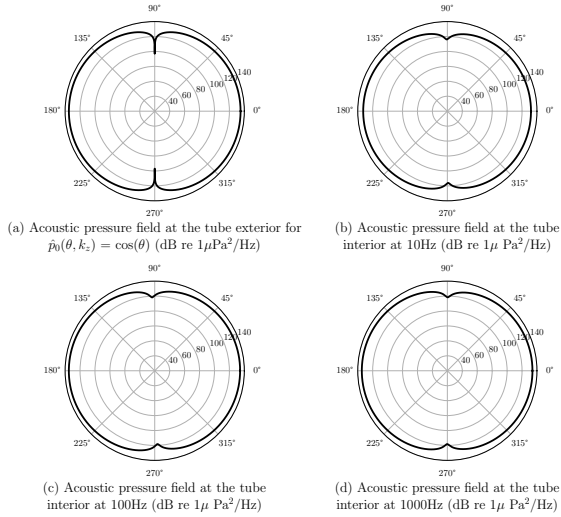


Fig. 7. (a) External acoustic pressure field  $\hat{p}_0(\theta, k_z) = \cos(\theta)$ , (b)-(d) Acoustic pressure field at the inner surface of the tube ( $r = a$ ) for different frequencies.

computed using the tube transfer function model [9] (see Fig. 9) and the axisymmetric model [11] (see Fig. 10). The elastic tube, inside fluid and hydrophone array parameters used for computation are given in Table. 1

It can be seen from Figs. 9 and 10 that the on-axis acoustic pressure computed using the 3D-VA model follows the external turbulent pressure excitation given in Fig. 8 - increasing upto and peaking at the convective

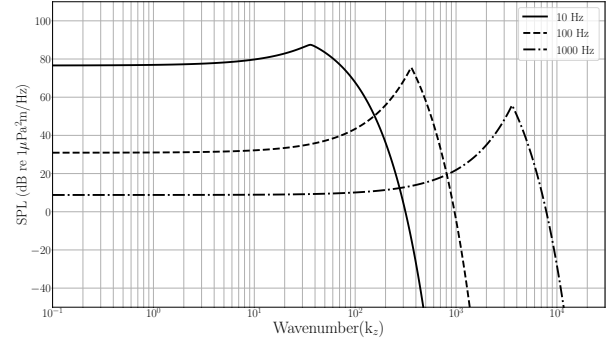


Fig. 8. The external turbulent pressure excitation at 5 knots over a tube of 40 mm diameter computed using the hybrid model (Eq. (18)).

Table 1. The elastic tube, interior fluid and the hydrophone array parameters used for estimation of flow noise inside the cylinder.

Property	Values
Tube diameter (m)	0.04
Tube thickness (m)	0.005
Tow speed/Flow velocity (knots)	5
Number of hydrophones	50
Length of hydrophone (m)	0.05
Hydrophone spacing (m)	0.25
Exterior fluid density ( $\text{kg/m}^3$ )	1000
Interior fluid density ( $\text{kg/m}^3$ )	800
Reference pressure ( $\mu\text{Pa}$ )	1

wavenumber ( $u_c = \omega/k_c$ ), and decreasing exponentially beyond. Thus, the flow noise inside the tube is dominated by the contribution from wavenumbers less than the convective wavenumber.

In the tube transfer function model (Fig. 9) and the axisymmetric model (Fig. 10) predictions, the peak occurs at a lower wavenumber than the convective wavenumber. For example, at 10 Hz, the peak occurs at 1.58 rad/m in the tube transfer function model and at 1.56 rad/m in the axisymmetric model. Note that the convective wavenumber at 10 Hz for 5 knots is  $k_c = 35.93 \text{ rad/m}$ . This smaller wavenumber where the first peak occurs in the transfer function and the axisymmetric models corresponds to the breathing mode wavenumber,

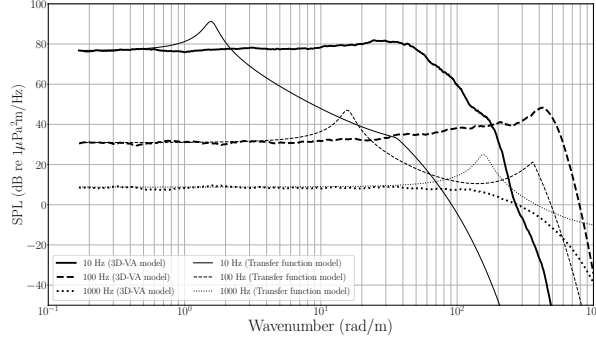


Fig. 9. Comparison of on-axis flow noise spectrum due to a turbulent pressure excitation at 5 knots over an elastic tube of diameter 40 mm computed using the present 3D-VA model and tube transfer function model [9].

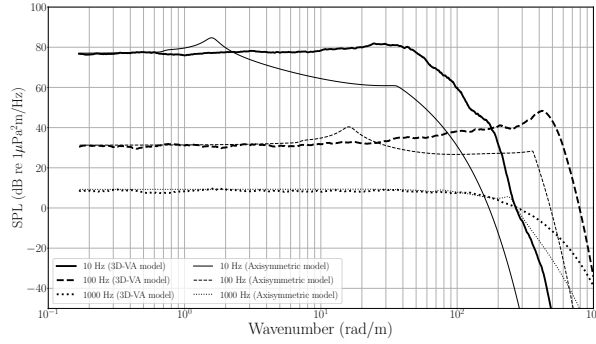


Fig. 10. Comparison of on-axis flow noise spectrum due to a turbulent pressure excitation at 5 knots over an elastic tube of diameter 40 mm computed using the present 3D-VA model and axisymmetric model [11].

$k_b$ , of the elastic tube given by [9]

$$k_b^2 = 2\rho_0\omega^2 R/Et. \quad (130)$$

In Eq. (130),  $\rho_0$  is the density of the inside fluid,  $R$  is the outer radius of the elastic tube,  $E$  is the Young's modulus of the tube and  $t$  is the thickness of the tube. The tube transfer function model and axisymmetric model consider only the breathing mode ( $n = 0$ ) variations while modelling the fluid-filled elastic tube. The present 3D-VA model considers both  $n = 0$  (breathing) and  $n = 1$  (first order) variations in the solid and fluid displacement fields. The absence of peaks at the breathing wavenumber in the present 3D-VA model indeed demonstrates a cumulative effect of including both  $n = 0$  and  $n = 1$  order terms in the fully-coupled vibroacoustic formulation. The same is the reason for the difference in flow noise spectrum be-

tween the 3D-VA model and the other models beyond the breathing wavenumber.

### 5.3 On-axis flow noise for external turbulent pressure excitation

This section presents the flow noise as heard by the hydrophones placed inside the fluid-filled elastic tube. The flow noise is computed using Eqs. (128) and (129). Note that the flow noise at a given frequency can be obtained by integrating the corresponding flow noise spectrum (Figs. 9 and 10) over the wavenumber. Fig. 11 shows the variation in flow noise with frequency, computed using the present fully-coupled 3D-VA model. It also depicts the flow noise predicted by the transfer function and the axisymmetric models. Note that in all the cases, the external turbulent pressure excitation is given by Eq. (18) (the hybrid model). The elastic tube, interior fluid and hydrophone parameters are given in Table. 1.

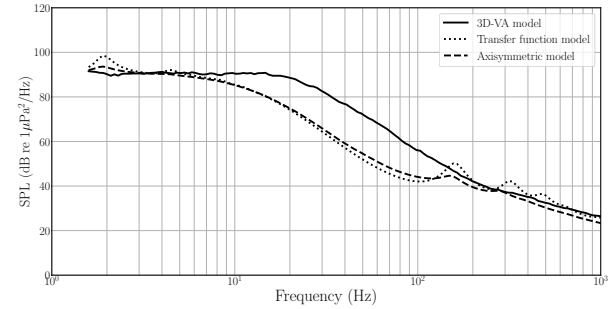


Fig. 11. The on-axis flow noise for an elastic tube of diameter 40 mm at 5 knots due to the turbulent pressure excitation computed using the present 3D-VA model, the tube transfer function model [9] and axisymmetric model [11].

It can be seen from Fig. 11 that the flow noise decreases with frequency. This decrease is attributed to the reduction in the external turbulent pressure excitation with frequency as shown in Fig. 8. As mentioned earlier, the 3D-VA model considers both  $n = 0$  (breathing) and  $n = 1$  variation in the acoustic pressure field. This results in a better flow noise prediction than the transfer function and axisymmetric models, where only the  $n = 0$  or the breathing wavenumber is considered. Note from Fig. 11 that the transfer function and the axisymmetric models underpredicts the flow noise in the mid frequency range (10 Hz - 200 Hz).

#### 5.4 On-axis flow noise for different tube diameters and tow speeds

In this section, the on-axis flow noise (Eqs. (128) and (129)) is computed for different elastic tube diameters and at different tow speeds. Fig. 12 shows the comparison of on-axis flow noise estimated for different elastic tube diameters at 5 knots and Fig. 13 shows the variation in the flow noise for a tube of 40 mm diameter at different tow speeds. The variation in flow noise is attributed to the changes in external turbulent pressure excitation with tube diameters and tow speeds as shown in Fig. 4 (the non-dimensional plot). It was shown in Fig. 4 that the increase in diameter or decrease in tow speed result in reduction in the non-dimensional power spectral density. This leads to a decrease in the on-axis flow noise inside the fluid-filled elastic tube with increasing tube diameter (Fig. 12)/decreasing tow speeds (Fig. 13).

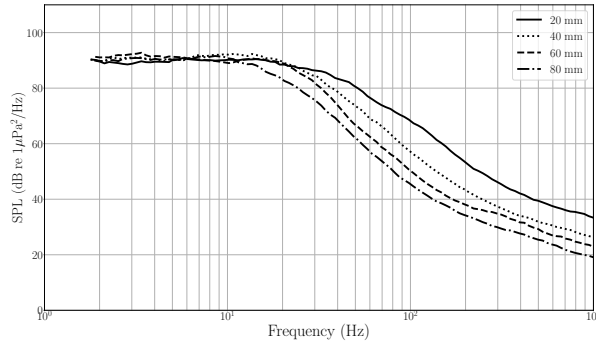


Fig. 12. Comparison of on-axis flow noise estimated using 3D-VA model, due to a turbulent pressure excitation at 5 knots over an elastic tube for different diameters.

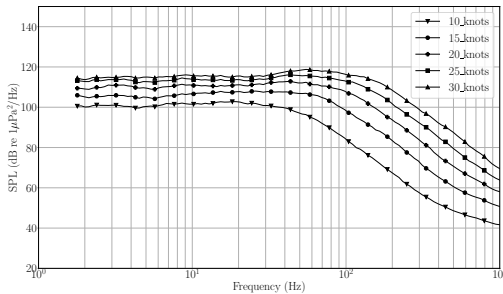


Fig. 13. Comparison of on-axis flow noise estimated using 3D-VA model, due to a turbulent pressure excitation over an elastic tube of 40 mm diameter at different tow speeds.

#### 6 CONCLUSIONS

A new semi-empirical (hybrid) model is developed for estimating the wavenumber-frequency spectrum of turbulent pressure for an axial flow past a solid cylinder. The hybrid model is derived using insights from different turbulent pressure semi-empirical models (Chase [4] and Abdelkader Frendi et al. [5]) and the experimental results of Unnikrishnan et al. [2]. The hybrid model predictions are found to be superior to the existing semi-empirical models and compares reasonably well with available experimental results.

A fully coupled three-dimensional vibroacoustic model (3D-VA model) is developed for computing the pressure field inside the fluid-filled elastic tube due to external turbulent pressure excitations. In this 3D-VA model, the structure (elastic tube) is modelled using the Navier-Lame equilibrium equations and the fluid inside the tube is modelled using acoustic wave equation. The developed 3D-VA model is first tested for an exterior harmonic pressure excitation having a known azimuthal variation. It is found that the interior pressure field follows the same azimuthal variation as that of the external excitation.

Next, the 3D-VA model is used in conjunction with the hybrid model of turbulent pressure spectrum to find the on-axis flow noise. The results are then compared with the on-axis flow noise estimated using the existing transfer function model [9] and the previous axisymmetric vibroacoustic model. Transfer function model and the axisymmetric model considers only the breathing mode ( $n = 0$ ) of the elastic tube but the 3D-VA model considers both  $n = 0$  (breathing) and  $n = 1$  (first order) variations in modelling the elastic tube and fluid inside the tube. Consequently, the two other models underpredict the flow noise compared to the 3D-VA model.

The on-axis flow noise is then estimated for different elastic tube diameters and at different tow speeds. At low frequencies, an increase in the tube diameter causes negligible variation in flow noise but at higher frequencies, the flow noise decreases with increase in the tube diameter. On increasing the tow speed, the flow noise is found to increase at all frequencies.

#### ACKNOWLEDGEMENTS

This research was supported by the Defence Research and Development Organisation, India. The authors express their sincere gratitude to Dr. Ganesh Natarajan and Dr. Pramod Kuntikana of the Indian Institute of Technology Palakkad for their invaluable support and guidance throughout this research. Special thanks also go to Dr. T. Santhanakrishnan, Mr. Sameer Abdul Azeez, Mr. Jineesh George, Mr. Samuel Theophilus, and Mr. An-

shath Hussain of the Naval Physical & Oceanographic Laboratory for their invaluable feedback and assistance with this project. We extend our gratitude to Prof. A. Seshadri Sekhar, Director of the Indian Institute of Technology Palakkad and Dr. Duvvuri Seshagiri, OS and Director of the Naval Physical & Oceanographic Laboratory, for their support in enabling this collaborative research.

## REFERENCES

- [1] Gopi, S., Felix, V. P., Sebastian, S., Pallayil, V., and Kuselan, S., 2010, "In-situ non-acoustic noise measurement system for towed hydrophone array," In 2010 IEEE Instrumentation Measurement Technology Conference Proceedings, pp. 913–916.
- [2] Unnikrishnan, K. C., Pallayil, V., Chitre, M. A., and Kuselan, S., 2011, "Estimated flow noise levels due to a thin line digital towed array," In OCEANS 2011 IEEE - Spain, pp. 1–4.
- [3] Corcos, G., 1963, "Resolution of pressure in turbulence," *The Journal of the Acoustical Society of America*, **35**(2), pp. 192–199.
- [4] Chase, D. M., 1981, Further modeling of turbulent wall pressure on a cylinder and its scaling with diameter, Dec.
- [5] Frendi, A., and Zhang, M., 2020, "A new turbulent wall-pressure fluctuation model for fluid–structure interaction," *Journal of Vibration and Acoustics*, **142**(2), p. 021018.
- [6] Goody, M., 2004, "Empirical spectral model of surface pressure fluctuations," *AIAA journal*, **42**(9), pp. 1788–1794.
- [7] Francis, R., Ebenezer, D., Bhattacharyya, S., and Sharma, R., 2023, "Estimation of wavenumber–frequency spectra of wall pressure due to turbulent flow over a flat plate using large-eddy simulation," *Physics of Fluids*, **35**(6).
- [8] Carpenter, A., and Kewley, D., 1983, "Investigation of low wavenumber turbulent boundary layer pressure fluctuations on long flexible cylinders," In Eighth Australasian Fluid Mechanics Conference, Vol. 28, 9A.
- [9] Knight, A., 1996, "Flow noise calculations for extended hydrophones in fluid-and solid-filled towed arrays," *The Journal of the Acoustical Society of America*, **100**(1), pp. 245–251.
- [10] Karthik, K., Jeyakumar, S., and Sebastin, J. S., 2021, "Numerical prediction of flow noise levels on towed sonar array," *Proceedings of the Institution of Mechanical Engineers, Part M: Journal of Engineering for the Maritime Environment*, **235**(2), pp. 600–606.
- [11] Jineesh, G., and Ebenezer, D. D., 2013, "Response of a linear array of hydrophones to flow-induced noise," In Acoustics, New Delhi - India, pp. 1–6.
- [12] Kuttan Chandrika, U., Pallayil, V., Lim, K. M., and Chew, C. H., 2014, "Flow noise response of a diaphragm based fibre laser hydrophone array," *Ocean Engineering*, **91**, pp. 235–242.
- [13] Huang, C., Li, H., and Li, N., 2020, "Flow noise spectrum analysis for vertical line array during descent in deep water," *Journal of Theoretical and Computational Acoustics*, **28**(04), p. 2050022.
- [14] Jordan, S. A., 2014, "On the Axisymmetric Turbulent Boundary Layer Growth Along Long Thin Circular Cylinders," *Journal of Fluids Engineering*, **136**(5), 03, p. 051202.
- [15] Sadd, M., 2014, *Elasticity: Theory, applications, and numerics, third edition* 01.
- [16] Achenbach, J., 2012, *Wave propagation in elastic solids* Elsevier.
- [17] Sekharipuram Sekar, R., Natarajan, G., Kuntikana, P., and Akkoorath Mana, A., 2024, "An axisymmetric model for predicting turbulent flow noise in towed sonar arrays," In 30<sup>th</sup> International Congress on Sound and Vibration, Amsterdam - Netherlands.